Engineering Research Journal
journal homepage: https://erj.journals.ekb.eg/

Development of a Hybrid Serial-Parallel Robot with 3DOF for Industrial Applications

Mohab. A. El-Sherif [1, *], Abdelkader A. Ibrahim [1], Mahmoud M. El-Samanty [1]

[1] Benha University - Faculty of Engineering - Department of Mechanical Engineering - Egypt

[*]Corresponding author E-mail: mohab.amr19@feng.bu.edu.eg

Abstract. The evolution of robotics has led to the development of hybrid serial-parallel robots that combine the precision and stability of parallel mechanisms with the adaptability of serial structures. This study focuses on designing and optimizing such a robot by integrating a series of joints into a two-axis parallel robot to enhance its operational range and versatility. Key objectives include optimizing arc and link lengths for improved workspace efficiency, determining suitable motor torque for effective payload management, deriving mathematical models for forward and inverse kinematics, and refining trajectory planning techniques. Advanced tools like SolidWorks for 3D modeling and MSC ADAMS for dynamic analysis are employed, with simulations used to evaluate angular velocity and motor torque. This study presents the design and simulation of a hybrid serial-parallel robot intended for precise pick-and-place operations. The research builds upon a comprehensive review of parallel robotics, through detailed 3D modeling and dynamic simulation, the system's behavior and potential capabilities are evaluated, offering insights into its suitability for high-speed industrial applications and future advancements in robotic technologies.

Keywords: Modified Two Axis Parallel Robot; Hybrid Serial Parallel Robot; Five Bar Mechanism; MSC Adams Simulation

DOI: 10.21608/erj.2025.371064.1224
Received 27 March 2025; Received in revised form 12 May 2025; Accepted 04 June 2025
Available online 01 September 2025

1 Introduction

The rapid advancements in robotics technology have significantly influenced industrial applications, particularly in the development of hybrid robotic systems. Hybrid serial-parallel robots, which combine the advantages of serial and parallel mechanisms, have been widely studied for their ability to enhance precision, rigidity, and operational flexibility in high-speed tasks such as material handling, packaging, and assembly [1][2][3][4][5]. These systems, especially those with three degrees of freedom (3DOF), have been recognized for their superior positioning capabilities and broader range of motion, making them highly suitable for diverse industrial environments [6][7]. Efforts have been made to optimize workspace utilization and avoid singularities through innovative designs, such as five-bar planar parallel robots [8][9]. Energy efficiency has also been improved by incorporating torsional springs and recuperative drive axles, which are capable of reducing motor torque demands during cyclic operations [10][11][12]. These advancements have positioned hybrid robots as a promising solution for modern industrial challenges.

The challenges associated with controlling hybrid mechanisms have been extensively addressed by researchers, with advanced strategies being proposed to enhance tracking performance and robustness. Computed torque control algorithms, for instance, have been implemented to improve the dynamic response of hybrid robots [13][14][15]. Adaptive and model-based control approaches have also been utilized to address the complexities of hybrid mechanisms, ensuring accurate trajectory tracking and operational stability [16][17]. To minimize energy consumption while maximizing performance, optimization techniques such as the Taguchi method have been applied to refine kinematic designs [18][19]. These developments underscore the importance of integrating control and design strategies to achieve efficient and reliable operation for industrial applications [20][21]. The focus on control methodologies has facilitated the successful application of hybrid robots in tasks requiring high precision and adaptability.

Energy efficiency and workspace optimization have emerged as critical factors in the development of hybrid robots. Design modifications, such as the inclusion of torsional springs and recuperative drive axles, have been shown to enhance energy savings during cyclic operations [22][23]. Workspace analysis has been extensively conducted to ensure static feasibility and stability. Numerical optimization techniques have been proposed to compute reachable workspaces, ensuring that designs align with specific industrial requirements [24][25][26]. Theoretical studies have also contributed to understanding the kinematic and dynamic behavior of these robots, enabling the development of robust mathematical models for precise operation [27][28]. By addressing these factors, hybrid robots have been optimized to meet the demands of modern industrial applications, where efficiency and precision are paramount.

Advancements in design and control methodologies have facilitated the integration of hybrid robotic systems into industrial settings. Strategies for actuator selection and dynamic balancing have been proposed to improve agility and adaptability in complex tasks [29][30]. Feedback control mechanisms have been shown to enhance operational precision while reducing strain on components, ensuring the longevity and reliability of robotic systems [31][32]. Additionally, artificial intelligence and machine learning techniques are being explored to enable real-time adaptation to changing task demands, further expanding the applicability of hybrid robots in manufacturing and assembly [33][41][]. These developments highlight the versatility and cost-effectiveness of hybrid systems in addressing the challenges of modern industrial operations.

This study aims to develop a 3DOF hybrid serial-parallel robot optimized for industrial applications, focusing on enhancing design flexibility, maximizing workspace reachability, and implementing robust control strategies. By integrating advanced mathematical modeling and energy-efficient designs, this research seeks to contribute to the growing body of knowledge in hybrid robotics [6][18][20][27] [39]. The findings are expected to provide a theoretical and practical foundation for future investigations, supporting the adoption of hybrid serial-parallel robots in diverse industrial environments [15][22][31] [40], a brief overview of the mechanical design modeling is provided in Section 2, followed by an explanation of the mathematical modeling approach in Section 3. The evaluation of the angular velocity simulation using MSC ADAMS is detailed in Section 4. Subsequently, Section 5 demonstrates the applicability of the developed framework through a pick-and-place simulation using MSC ADAMS for the hybrid serial-parallel robot. The results of the proposed method are thoroughly analyzed in Section 6. Finally, the key findings and conclusions of the work are summarized in Section 7.

2 Modeling of Mechanical Design

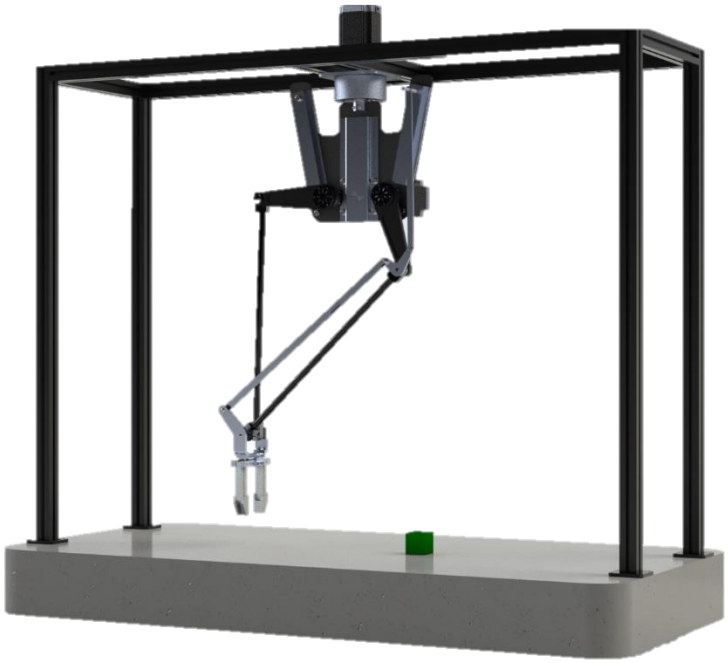

Fig. 1. A Full description of the rendered 3D Model for the Hybrid Serial-Parallel Robot for Precision Pick-and-Place Operations

2.1. Introduction

This paper explores the design as illustrated in **Fig. 1 and analyzes** a hybrid serial-parallel robot specifically developed for precision pick-and-place tasks in industrial settings. By combining the benefits of serial and parallel mechanisms, the robot achieves superior efficiency, accuracy, and adaptability. The study delves into the robot's mechanical design, actuation systems, and manufacturing specifications, supported by simulation data. In industrial automation, pick-and-place operations require exceptional precision and reliability. Hybrid robotic systems, which integrate serial and parallel configurations, have emerged as a compelling solution to meet these stringent requirements. These systems capitalize on the strengths of both mechanisms, offering increased load capacity, reduced positional errors, and enhanced dynamic stability. This paper outlines the design methodology, structural composition, and functional capabilities of a hybrid serial-parallel robot engineered to meet these operational demands.

2.2. Mechanical Design

The structural frame of the robot serves as its foundational support, accommodating all components while ensuring robustness and stability. Constructed from lightweight aluminum extrusions, the frame is designed to provide a high strength-to-weight ratio along with excellent corrosion resistance. Its modular design simplifies assembly and maintenance while also enabling scalability, making it suitable for a wide range of industrial applications. The actuation system of the robot comprises a combination of motors strategically positioned to deliver precise control and efficient power distribution. A central motor, located at the top of the structure, facilitates 360° rotational movement around the vertical axis, while two lateral motors ensure stability and enable precise lateral adjustments, resulting in synchronized and balanced motion.

The robot’s parallel arm mechanism is composed of rigid aluminum arms connected through pivot joints. This configuration reduces stress on individual joints and ensures even torque distribution, enhancing precision and operational efficiency. Furthermore, the parallel arms are designed to minimize deflection, maintaining positional error, trajectory tracking deviation, and repeatability even during high-speed operations. At the end of the robot, the end effector is equipped with a gripper mechanism capable of handling objects up to 4 cm x 4 cm in size and a maximum payload of 200 grams. The gripper is highly versatile and can be customized to suit specific applications, including handling delicate or irregularly shaped objects. The base platform, constructed from concrete, provides a stable and immovable foundation for the robot. This robust design minimizes vibrations and ensures consistent performance during dynamic operations, further enhancing the robot’s reliability.

2.3. Manufacturing Specifications

The hybrid serial-parallel robot is built with performance and durability in mind. Its structure uses lightweight aluminum for the frame and arms, stainless steel for bearings to ensure long-lasting operation, and a concrete base for enhanced stability and vibration dampening. The modular and scalable design allows easy maintenance and adaptability to different payloads or working volumes. The robot includes three stepper motors with encoders, high-precision joints, aluminum arms, and a customizable end effector. Sensors like encoders and limit switches ensure precise control, while shielded wiring supports reliable operation. Electronics include motor drivers, a power supply, and a microcontroller board. The system runs inverse kinematics software to enable Smooth motion control, while bushings and bearings ensure smooth joint movements. Additionally, the robot’s control software incorporates inverse kinematics algorithms, which are critical for accurate motion control and task execution, as illustrated in **Fig. 2.**

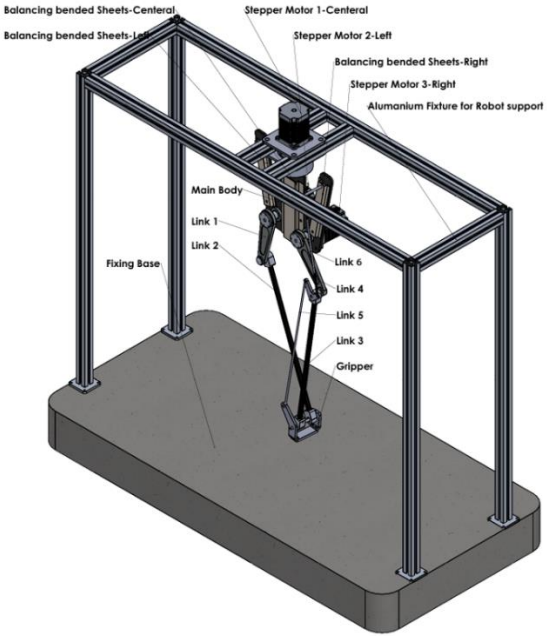

Fig. 2. A Schematic for the two-axis parallel robot that was designed using Solidworks software

2.4. Assembly instructions with full description

The robot's assembly starts with the main structural base, which includes two stepper motors, radial bearings, and reinforced metal sheets for stability. The vertical motor is then added to provide full 360° rotation, mounted on a thrust bearing, and fixed to an aluminum frame. Next, the structure is integrated and fastened with bolts and nuts. In the following stages, the arm links (Links 1 to 4) are assembled with radial bearings to allow smooth rotation. Link 2 and Link 3 are connected to the gripper support, and radial bearings are used for precise motion. Finally, a restriction mechanism—made of Links 5 and 6 and a connecting joint—is installed to enhance control. The entire assembly is visually represented in Fig. 3.

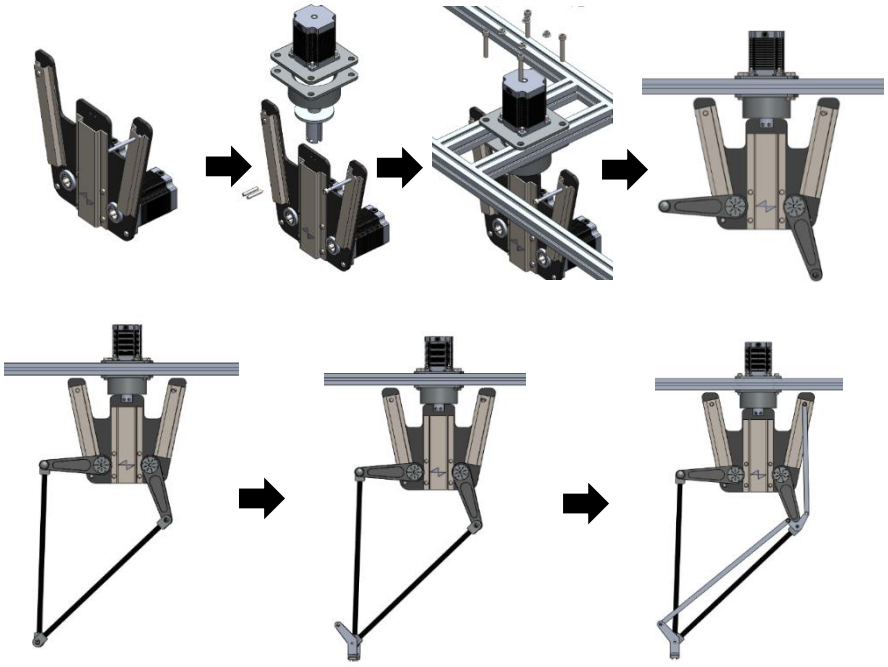

Fig. 3. Step-by-Step Guide to the Assembly and Installation Process

3 Mathematical Modeling

Kinematic analysis is necessary to build the mathematical model of the robot. The aim is to establish the relation between joint angles and the coordinates of the end-effector. The two-axis parallel robot with revolute joints and symmetric design is considered. The length of the links and the fixed joints coordinates are shown in **Fig. 4.** Two actuators are located at B and F, having rotation angles denoted by θ2 and θ3, respectively, and also the main actuator that is located at A, having a rotation angle around the Y-axis denoted by θ1. The end-effector is fixed at D.

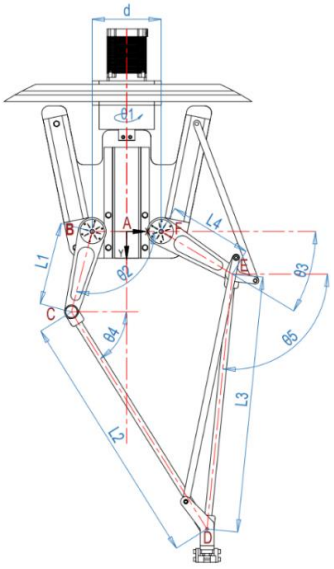

Fig. 4. Schematic for the two-axis parallel robot

The following vector equation can be derived: -

$$\overrightarrow{BD}=\overrightarrow{AB}+\overrightarrow{BC}+\overrightarrow{CD}=\overrightarrow{AE}+\overrightarrow{EF}+\overrightarrow{FD}$$

$$\begin{Bmatrix} X_D \\ Y_D \end{Bmatrix}=\begin{Bmatrix} -{}^{d}/_{2} + L1\cos\theta2 + L2\cos\theta4 \\ L1\sin\theta2 + L2\sin\theta4 \end{Bmatrix} = \begin{Bmatrix} {}^{d}/_{2} + L4\cos\theta3 + L3\cos\theta5 \\ L4\sin\theta3 + L3\sin\theta5 \end{Bmatrix} \quad (1)$$

3.1. Forward Kinematic: -

Given the joint angles ($\theta2$, $\theta3$), eliminating terms $\theta4$ and $\theta5$ in Eqn. (1) leads to the coordinates of the end-effector at P as follows: -

$$X_D = -{}^{d}/_{2} + L1\cos\theta2 + L2\cos\theta4 = {}^{d}/_{2} + L4\cos\theta3 + L3\cos\theta5 \quad (2)$$

$$Y_D = L1\sin\theta2 + L2\sin\theta4 = L4\sin\theta3 + L3\sin\theta5 \quad (3)$$

We can split equation 2 into two parts as follows:

$$X_D = -{}^{d}/_{2} + L1\cos\theta2 + L2\cos\theta4 \quad (4)$$

From equation 4, we can get:

$$\cos\theta4 = \frac{X_D + {}^{d}/_{2} - L1\cos\theta2}{L2} \quad (5)$$

$$\theta4 = \cos^{-1}\frac{X_D + {}^{d}/_{2} - L1\cos\theta2}{L2} \quad (5)$$

$$X_D = {}^{d}/_{2} + L4\cos\theta3 + L3\cos\theta5 \quad (6)$$

From equation 6, we can get:

$$\cos\theta5 = \frac{X_D - {}^{d}/_{2} - L4\cos\theta3}{L3} \quad (7)$$

$$\theta5 = \cos^{-1}\frac{X_D - {}^{d}/_{2} - L4\cos\theta3}{L3} \quad (8)$$

We can split equation 3 into two parts as follows:

$$Y_D = L1\sin\theta2 + L2\sin\theta4 \quad (9)$$

From equation 9, we can get:

$$\sin\theta4 = \frac{Y_D - L1\sin\theta2}{L2} \quad (10)$$

$$\theta4 = \sin^{-1}\frac{Y_D - L1\sin\theta2}{L2} \quad (11)$$

$$Y_D = L4\sin\theta3 + L3\sin\theta5 \quad (12)$$

From equation 12, we can get:

$$\sin\theta5 = \frac{Y_D - L4\sin\theta3}{L3} \quad (13)$$

$$\theta5 = \sin^{-1}\frac{Y_D - L4\sin\theta3}{L3} \quad (14)$$

From equations 7 & 10, we can get:

$$\tan\theta4 = \frac{\sin\theta4}{\cos\theta4}$$

$$\tan\theta4 = \frac{Y_D - L1\sin\theta2}{L2} \Big/ \frac{X_D + {}^{d}/_{2} - L1\cos\theta2}{L2}$$

We can simplify equation 14:

$$\tan\theta4 = \frac{Y_D - L1\sin\theta2}{X_D + {}^{d}/_{2} - L1\cos\theta2} \quad (15)$$

$$\theta4 = \tan^{-1}\frac{Y_D - L1\sin\theta2}{X_D + {}^{d}/_{2} - L1\cos\theta2} \quad (16)$$

From equations 5 & 9, we can get:

$$\tan\theta5 = \frac{\sin\theta5}{\cos\theta5}$$

$$\tan\theta5 = \frac{Y_D - L4\sin\theta3}{L3} \Big/ \frac{X_D - {}^{d}/_{2} - L4\cos\theta3}{L3} \quad (17)$$

We can simplify equation 14:

$$\tan\theta5 = \frac{Y_D - L4\sin\theta3}{X_D - {}^{d}/_{2} - L4\cos\theta3} \quad (18)$$

$$\theta5 = \tan^{-1}\frac{Y_D - L4\sin\theta3}{X_D - {}^{d}/_{2} - L4\cos\theta3} \quad (19)$$

Let's substitute equation 4 for equation 16

$$X_D = -{}^{d}/_{2} + L1\cos\theta2 + L2\cos(\tan^{-1}\frac{Y_D - L1\sin\theta2}{X_D + {}^{d}/_{2} - L1\cos\theta2})$$

$$Y_D = L1\sin\theta2 + L2\sin(\tan^{-1}\frac{Y_D - L1\sin\theta2}{X_D + {}^{d}/_{2} - L1\cos\theta2})$$

We obtained equation 20: -

$$X_D = -{}^{d}/_{2} + L1\cos\theta2 + L2\cos(\tan^{-1}\frac{L4\sin\theta3 + L3\sin\theta5 + -L1\sin\theta2}{L4\cos\theta3 + L3\cos\theta5 + d - L1\cos\theta2}) \quad (20)$$

We obtained equation 21: -

$$Y_D = L1\sin\theta2 + L2\sin(\tan^{-1}\frac{L4\sin\theta3 + L3\sin\theta5 + -L1\sin\theta2}{L4\cos\theta3 + L3\cos\theta5 + d - L1\cos\theta2}) \quad (21)$$

The stepper motors do not actuate the joints C and E. For that reason, the angles $\theta4$ and $\theta5$ are dependent, and $\theta2$ and $\theta3$ are independent. The Last equations have been adapted from Vathan et al. [34]: -

$$\theta4 = \sin^{-1}(\frac{L3\sin\theta5 + L4\sin\theta3 - L1\sin\theta2}{L2}) \quad (22)$$

$$\theta5 = 2\tan^{-1}(\frac{A \pm \sqrt{A^2 + B^2 - C^2}}{B - C}) \quad (23)$$

The value of A, B, and C is found using the expressions:

$$A = 2L3\ L4\ sin\theta3 - 2L1\ L3cos\theta3$$

$$B = 2L3\ d - 2\ L1\ L3\ cos\theta2 + 2\ L3\ L4\ cos\theta3$$

$$C = L1^2 - L2^2 + L4^2 + L3^2 + d^2 - L1\ L4\ sin\theta2\ sin\theta3 - 2\ L1\ d\ \ cos\theta2 + 2\ L4\ d\ \ cos\theta3 - 2\ L1\ L4\ \ cos\theta2\ cos\theta3$$

If we consider that theta 1 is not equal to 0, we have to get the following Transformation matrix: -

$$T = \begin{bmatrix} C\theta1 & 0 & S\theta1 \\ 0 & 1 & 0 \\ -S\theta1 & 0 & C\theta1 \end{bmatrix} * \begin{bmatrix} \boldsymbol{X_D} \\ \boldsymbol{Y_D} \\ 0 \end{bmatrix} = \begin{bmatrix} C\theta1 * \boldsymbol{X_D} \\ \boldsymbol{Y_D} \\ -S\theta1 * \boldsymbol{X_D} \end{bmatrix} \quad (24)$$

3.2. Inverse Kinematics: -

The inverse kinematics equations provide solutions for the joint angles $\theta2$ and $\theta3$ corresponding to each coordinate. X_D and Y_DWithin the robot's workspace, as illustrated in **Fig. 5.** These equations were derived using geometric methods, with the essential robot dimensions necessary for calculating the inverse kinematics also depicted in Figure 3. The inverse kinematics have been adapted from Shen et al.'s conference paper [35].

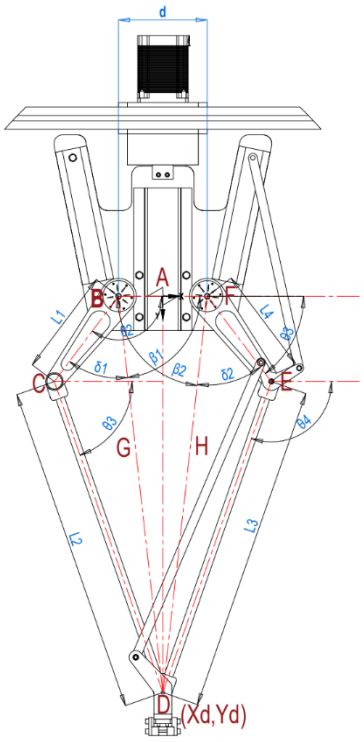

Fig 5. A Schematic for the two-axis parallel robot used for inverse kinematic analysis

$$\begin{cases} \theta 2 = \delta 1 + \beta 1 \\ \theta 3 = 180 - \delta 2 + \beta 2 \end{cases}$$

Firstly, we will illustrate the left-hand side: -

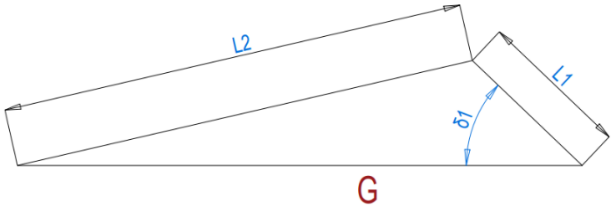

Fig 6. Schematic Diagram of the Left-Hand Side of the Two-Axis Parallel Robot for Inverse Kinematic Analysis

If we apply the cosine rule, we will get: -

$$\boldsymbol{L_2}^2 = \boldsymbol{L_1}^2 + G^2 - 2 * \boldsymbol{L_1} * G * cos\,\delta 1$$

$$\delta 1 = cos^{-1} \frac{-\boldsymbol{L_2}^2 + \boldsymbol{L_1}^2 + G^2}{2 * \boldsymbol{L_1} * G}$$

$$G = \sqrt{(x + \frac{d}{2})^2 + Y^2}$$

$$\beta 1 = tan^{-1} \frac{Y}{x + \frac{d}{2}}$$

$$\theta 2 = \delta 1 + \beta 1$$

$$\theta 2 = cos^{-1}\frac{-{L_2}^2+{L_1}^2+G^2}{2*L_1*G} + tan^{-1}\frac{Y}{x+\frac{d}{2}} \quad (25)$$

Secondly, we will illustrate the right-hand side: -

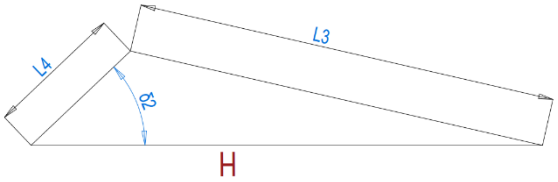

Fig 7. Schematic Diagram of the Right-Hand Side of the Two-Axis Parallel Robot for Inverse Kinematic Analysis

If we apply the cosine rule, we will get: -

$$\boldsymbol{L_3}^2 = \boldsymbol{L_4}^2 + H^2 - 2 * \boldsymbol{L_4} * H * cos\,\delta 2$$

$$\delta 2 = cos^{-1}\frac{-\boldsymbol{L_3}^2 + \boldsymbol{L_4}^2 + H^2}{2 * \boldsymbol{L_4} * H}$$

$$H = \sqrt{(x - \frac{d}{2})^2 + Y^2}$$

$$\beta 2 = tan^{-1}\frac{Y}{x - \frac{d}{2}}$$

$$\theta 3 = 180 - \delta 2 - \beta 2$$

$$\theta 3 = 180 - cos^{-1}\frac{-{L_3}^2+{L_4}^2+H^2}{2*L_4*H} - tan^{-1}\frac{Y}{x-\frac{d}{2}} \quad (26)$$

Thirdly, to get the Theta 1 ($\theta 1$):

- There are Key Points that have to be addressed:
  - Inverse Kinematics of the 5-Bar Mechanism (2 DOF): The inverse kinematics of a 5-bar mechanism involves finding the joint angles $\theta 2$ and $\theta 3$ that position the end-effector at a given point (X, Y) in 2D space. These angles are functions of X and Y, typically derived from geometric or trigonometric relationships within the parallel mechanism.
  - Adding the Rotation $\theta 1$ Around the Y-Axis: The rotation θ1\theta_1θ1 adds a third degree of freedom by rotating the entire 5-bar mechanism in 3D space. This rotation affects the position of the end-effector in the XZ-plane, introducing a new dimension for which the inverse kinematics can be accounted.
- Inverse Kinematics with Rotation Around Y-Axis:
  Given that: -
  - $\theta 2$ and $\theta 3$ are calculated using the 2-DOF inverse kinematics of the 5-bar mechanism (functions of X and Y).
  - $\theta 1$: Rotation around the Y-axis (adding a 3rd DOF).

The rotation matrix around the Y-axis is: -

$$Ry(\theta 1) = \begin{bmatrix} \boldsymbol{cos\,\theta 1} & 0 & \boldsymbol{Sin\,\theta 1} \\ 0 & 1 & 0 \\ \boldsymbol{-Sin\,\theta 1} & 0 & \boldsymbol{cos\,\theta 1} \end{bmatrix} (27)$$

▪ End-Effector Position Transformation:

To account for the rotation $\theta 1$, the authors relate the 2D position of the end-effector in the XY-plane to its 3D position in the XZ-plane after rotation.

Let:

- X′, Y′, Z′ are the coordinates of the end-effector in the rotated frame.
- X, Y, Z are the coordinates in the original frame.

The transformation is:

$$\begin{bmatrix} X' \\ Y' \\ Z' \end{bmatrix} = Ry(\theta 1) \begin{bmatrix} X \\ Y \\ 0 \end{bmatrix} = \begin{bmatrix} cos(\theta 1) . X \\ Y \\ -Sin(\theta 1). X \end{bmatrix} \quad (28)$$

Thus, the end-effector position becomes:

$$X' = Cos(\theta 1) . X \quad (29)$$

$$Z' = -Sin(\theta 1) . X \quad (30)$$

▪ Solving for θ1\theta_1θ1:

To solve for $\theta 1$, you can use the fact that the end-effector must meet specific spatial constraints. You may want to control where the end-effector should be in 3D space (X′, Y′, Z′). From the above equations:

$$\theta 1 = arctan(\frac{-Z'}{X'}) . \quad (31)$$

In this case, X′ and Z′ are derived from the desired position of the end-effector and the 2-DOF kinematics of the 5-bar mechanism. The rotation $\theta 1$ aligns the mechanism in 3D.

4 Angular Velocity Evaluation Simulation Using MSC ADAMS

In this section, the authors present the simulation process and results using MSC ADAMS, a powerful tool for analyzing dynamic systems. The simulation was conducted to evaluate the performance of the robotic system, specifically focusing on generating torque plots and angular velocity profiles for each motor position. To optimize the simulation process, the CAD model was simplified, ensuring efficient computation while maintaining the positional error, trajectory tracking deviation, and repeatability of the results. After importing the model into MSC ADAMS, all joints and motor positions were carefully configured. The results obtained provide valuable insights into the torque requirements and motor behavior, as well as the overall dynamic performance of the system. These outputs are essential for refining the robot's design and ensuring its operational efficiency.

Initially, the model was simplified to streamline the simulation process within the software. Afterward, the authors configured all the joints and positioned the motors in the imported CAD model, as demonstrated in **Fig. 8.**

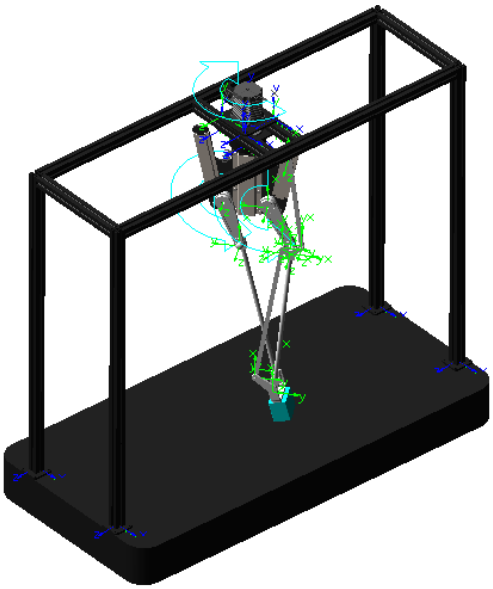

Fig. 8. A Schematic for the configuration of the joints and the position of the motors.

Subsequently, the authors conducted a simulation using a 300-gram payload, representing the maximum load capacity, to assess the robot's performance and select the most suitable motor for industrial applications. This test allowed us to evaluate the motor's torque and angular velocity under real-world operating conditions, ensuring that the chosen motor can handle the required load efficiently and reliably. The simulation results provide critical data for optimizing motor selection and enhancing the robot's performance in industrial environments.

Fig. 9 depicts the hybrid serial-parallel robot's initial position at the start of the simulation. This starting point serves as the baseline for analyzing the robot's motion and motor performance over time.

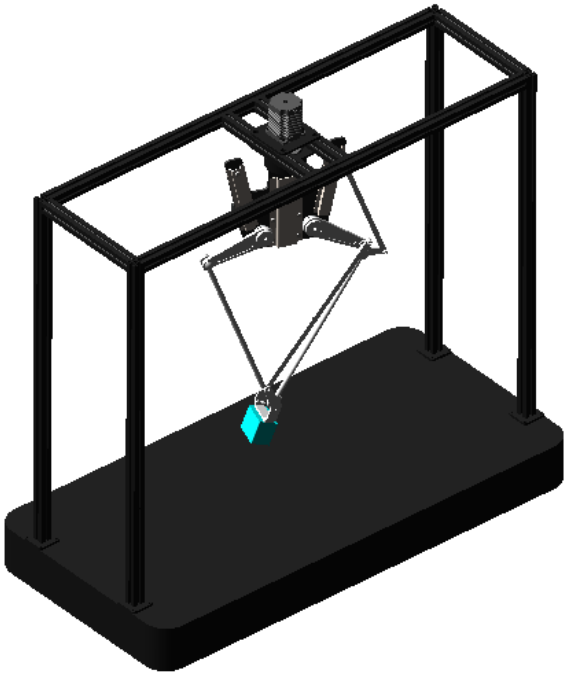

Fig. 9. A Schematic for the initial position of the hybrid serial-parallel robot through the simulation process.

Fig. 10 shows the robot's final position after completing the 10-second simulation. By comparing the initial and final positions, the authors can assess the changes in angular velocity for each motor and evaluate the overall movement of the system.

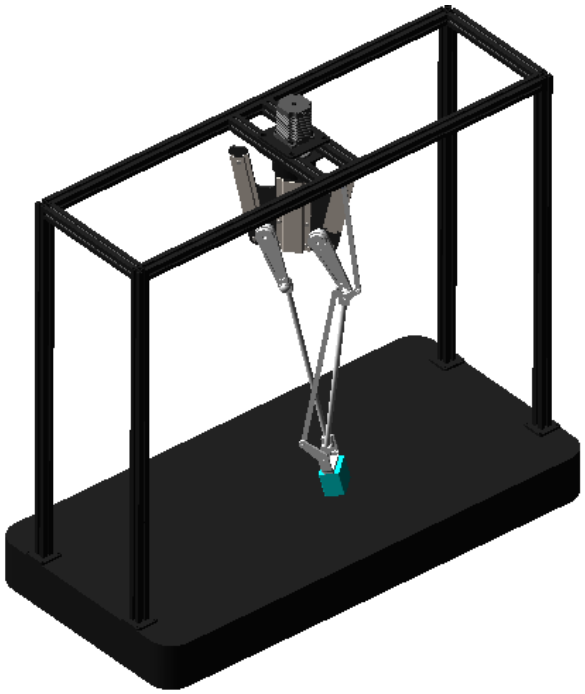

Fig. 10. A Schematic for the final position of the hybrid serial-parallel robot through the simulation process.

The simulation results shown in Fig. 11 below indicate that the axial motor experiences a significant peak in angular velocity, reaching approximately 320 deg/sec shortly after the simulation begins, before quickly stabilizing near zero at around 1 second. This suggests that the axial motor is responsible for the primary motion in the system. In contrast, the two horizontal motors display much lower angular velocities, with peaks not exceeding 35 deg/sec, and also stabilize quickly.

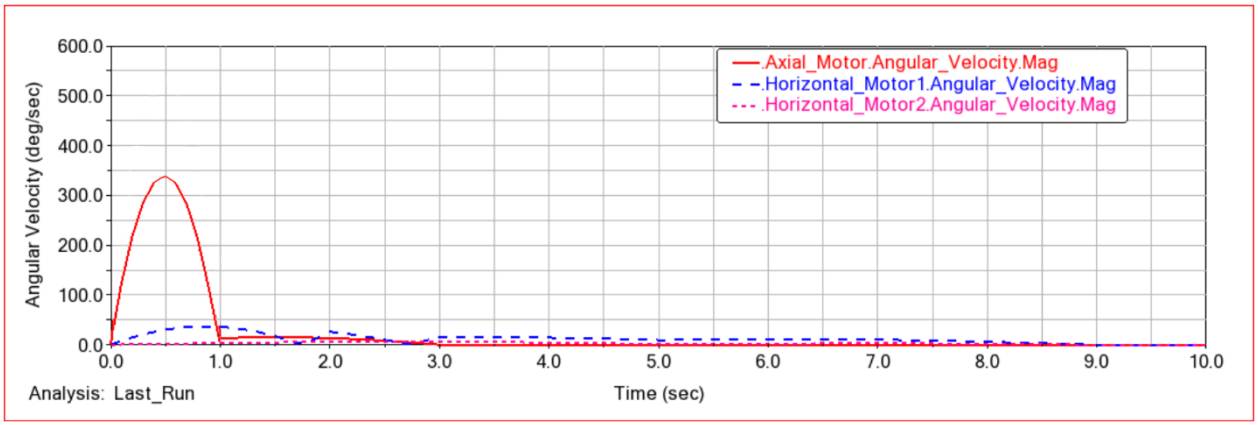

Fig. 11. A Schematic for the Angular velocity of the axial and two horizontal motors.

These findings suggest that the axial motor handles the majority of the movement, requiring higher torque and speed, while the horizontal motors provide more limited rotational input for fine-tuned adjustments or stabilization.

5 Pick and place simulation using MSC ADAMS for the Hybrid Serial-Parallel Robot.

In this simulation, the hybrid serial-parallel robot is tasked with performing a pick-and-place operation involving a 4 cm x 4 cm stainless steel box weighing 200 grams. This payload serves as the safe maximum weight capacity for the robot's current configuration, according to the last simulation mentioned in section 4. The simulation is designed to evaluate the robot's ability to handle such a load while maintaining precision and stability throughout the pick-and-place cycle. The performance of the motors, joints, and end-effector is analyzed to ensure smooth movement and repeatability in handling the object, which represents a real-world industrial application for the robot.
The simulation begins with the preparation of the exported CAD model from the Solidworks program, shown in Fig. 12, as discussed in the previous section, which is simplified to facilitate efficient processing in MSC ADAMS. Next, the trajectory definition phase involves mapping the end-effector's path from the initial pick-up to the final placement point. The trajectory is carefully designed to optimize the robot's degrees of freedom, ensuring smooth transitions and minimizing operational time and energy consumption. This step ensures that the payload— a 4 cm x 4 cm stainless steel box weighing 200 grams— is handled with precision.

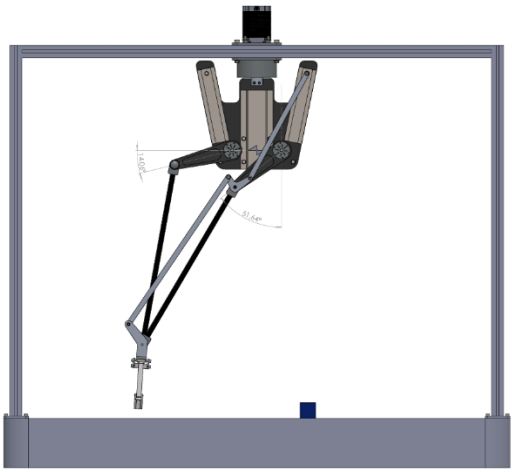

Fig 12. A Schematic for the exported CAD Model from the SolidWorks program

In the motor and joint configuration stage, torque and velocity profiles are assigned to the motors and joints. These are calibrated to control the robot's motion, delivering the necessary power and repeatability to complete the operation smoothly. This configuration ensures that the robot can successfully handle its maximum payload while maintaining precise control over its movements as shown the below Figures (12, 13, 14, 15) the pick and place simulation execution, the MSC ADAMS software computes the dynamic interactions, such as the angular velocities and forces acting on each motor and joint. This stage provides a clear visual and numerical analysis of the robot's efficiency in completing the task.
In the initial position, the hybrid serial-parallel robot is set in its home position, which is shown in **Fig. 13.**

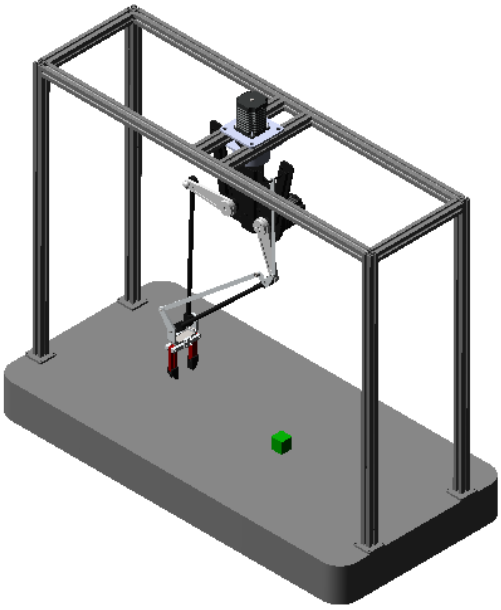

Fig 13. The home position of the hybrid serial-parallel robot

Above the target object, a 4 cm x 4 cm stainless steel box weighing 200 grams. The robot's end-effector is aligned precisely with the object, preparing to execute the pick action. The arms are extended, and the motors are ready to engage for the downward motion in **Fig. 14.** The robot has successfully grasped the stainless-steel box using the end-effector. In this mid-operation stage, the robot's arms begin to retract while lifting the object. The movement showcases the coordinated action of the serial and parallel links, smoothly raising the object from the platform to begin the transition towards the placement position.

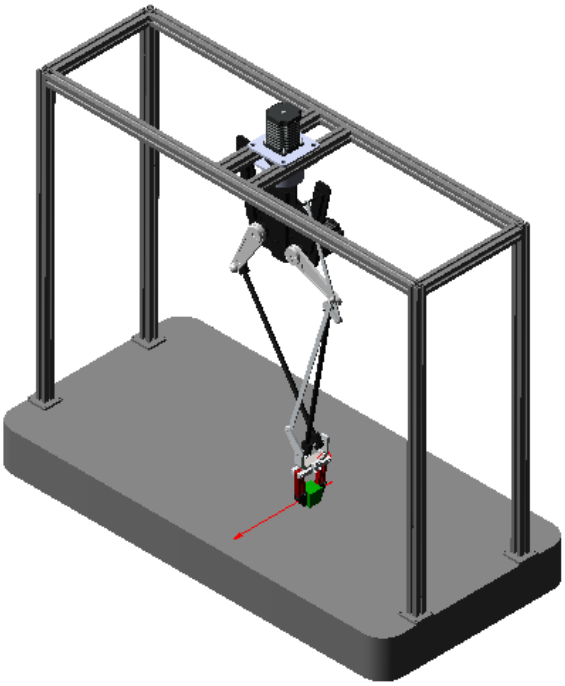

Fig. 14. The robot has successfully grasped the stainless-steel box.

In this stage of the pick-and-place process, the robot has moved the stainless-steel box to the designated placement area, shown in **Fig. 15.** The end-effector prepares to release the object, demonstrating the successful completion of the task. The robot's links and motors work in tandem to place the object

accurately at the targeted location, highlighting its precision and control in handling the maximum payload.

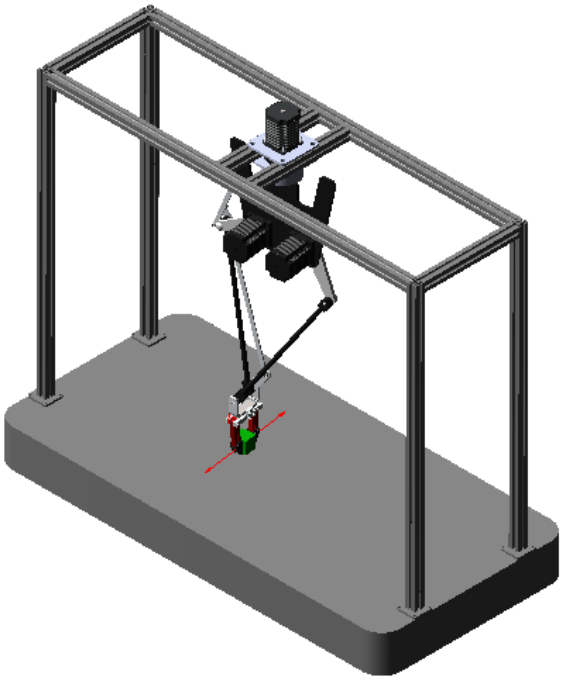

Fig 15. The robot has successfully dropped the box in the target position and returned to its home position

Finally, the hybrid parallel-serial robot returns to its home position after dropping the stainless-steel box in the target position to be ready for a future task, as shown in Fig. 16 below**.**

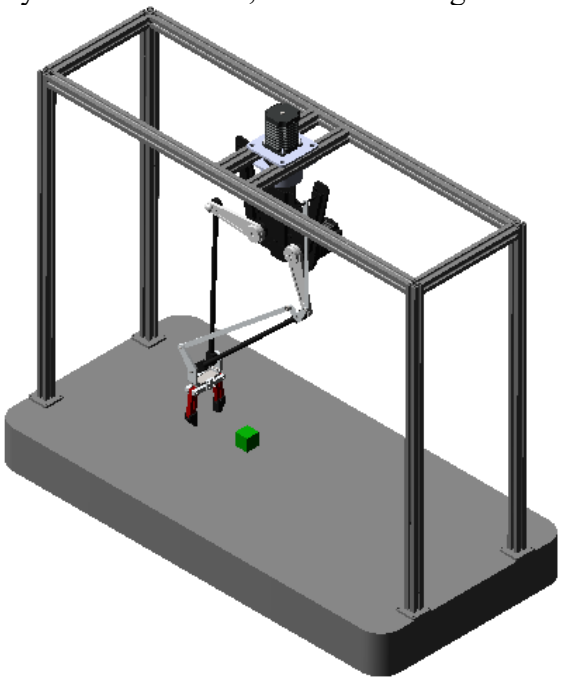

Fig. 16. The robot has successfully dropped the box in the target position and returned to its home position.

6 Results

The following results detail the performance of the hybrid serial-parallel robot's motors during a simulated pick-and-place operation involving a stainless-steel box. This analysis provides insights into motor coordination, angular velocity, and torque dynamics essential for evaluating motor capability, stabilization, and precision during each phase of the task. The plots in **Fig.17.** represents the results from the pick-and-place simulation of the stainless-steel box, highlighting the angular velocities of the three motors: CENT_MOT (central vertical motor), LM_MOT (left motor), and RM_MOT (right motor). The central motor shows periodic peaks, reaching up to 275 deg/sec, indicating it is responsible for the primary 360-degree rotation around the vertical axis during the lifting and lowering phases of the task. In contrast, the left and right motors exhibit lower angular velocities, peaking at 100 deg/sec and 73 deg/sec, respectively, with oscillations that gradually decrease over time. This pattern suggests that both the left and right motors play a stabilizing role, making fine adjustments to ensure lateral balance and precision during the pick-and-place operation. Overall, the simulation results demonstrate effective motor coordination, with the central motor driving the main motion and the lateral motors contributing to stabilization and accuracy. To ensure realistic and dynamically stable motion during the pick-and-place operation, a predefined trajectory plan was implemented for the end-effector. A trapezoidal velocity profile was adopted, which is widely used in industrial robotic systems to achieve smooth acceleration and deceleration. The motion was executed along a linear path in Cartesian space, with the maximum linear velocity set at 200 mm/s and the maximum linear acceleration defined as 500 mm/s². These values were selected to reflect typical operational conditions for precision pick-and-place tasks. The trajectory was applied through a time-dependent motion function within the MSC ADAMS environment, allowing for controlled changes in position, velocity, and acceleration. By employing this motion plan, abrupt dynamic loads were minimized, and more accurate assessments of angular velocity and torque requirements were enabled. This approach contributed to the improved performance stability observed in the simulation results.

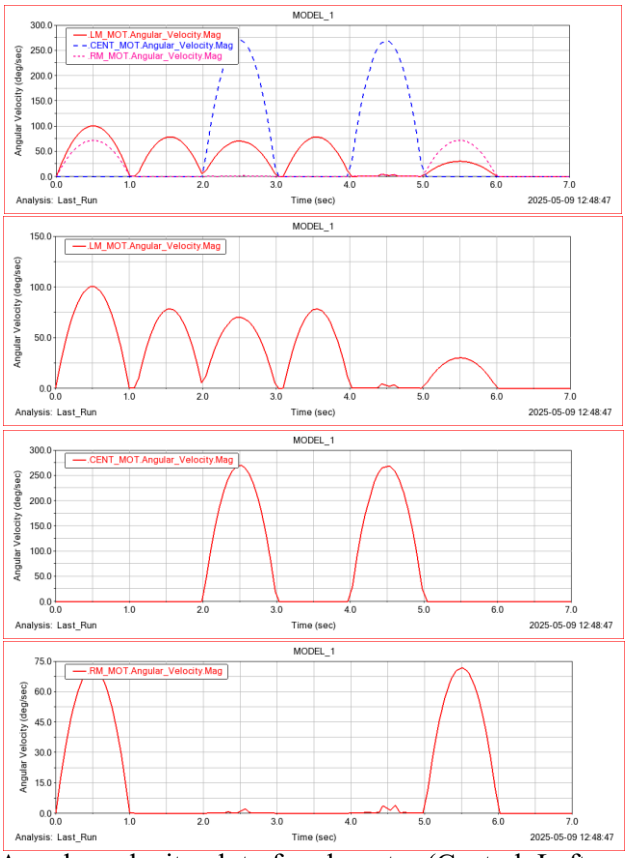

Fig. 17. Angular velocity plot of each motor (Central, Left, and Right Motors)

Additionally, the pick-and-place simulation, the authors obtained torque plots for each motor, providing key insights into the forces exerted during the operation. These torque plots help in understanding the load distribution among the central, left, and right motors, ensuring the motors are capable of handling the required forces for lifting, placing, and stabilizing the stainless-steel box during the task. The torque data will be crucial for assessing motor performance, selecting appropriate motor specifications, and ensuring efficient and reliable operation in industrial applications. The torque plots provide a comprehensive analysis of motor performance during the pick-and-place simulation that shown in the below **Fig.18.** The left motor (LM_MOT) exhibits an initial torque peak of approximately 1500 N·mm, followed by moderate fluctuations within the first 3 seconds, indicating its role in providing periodic corrective forces to stabilize lateral movement. The central motor (CENT_MOT), which is responsible for 360-degree rotation around the vertical axis, shows a significant torque peak at around 9000 N·mm during the rotation around the vertical axis phase. Unlike the lateral motors, the central motor exhibits larger, consistent fluctuations after this peak, reflecting the motor's role in maintaining the stability of the robot's positioning. The right motor (RM_MOT) peaks at approximately 1240 N·mm, also playing a key role in stabilizing lateral movements, mirroring the behavior of the left motor.

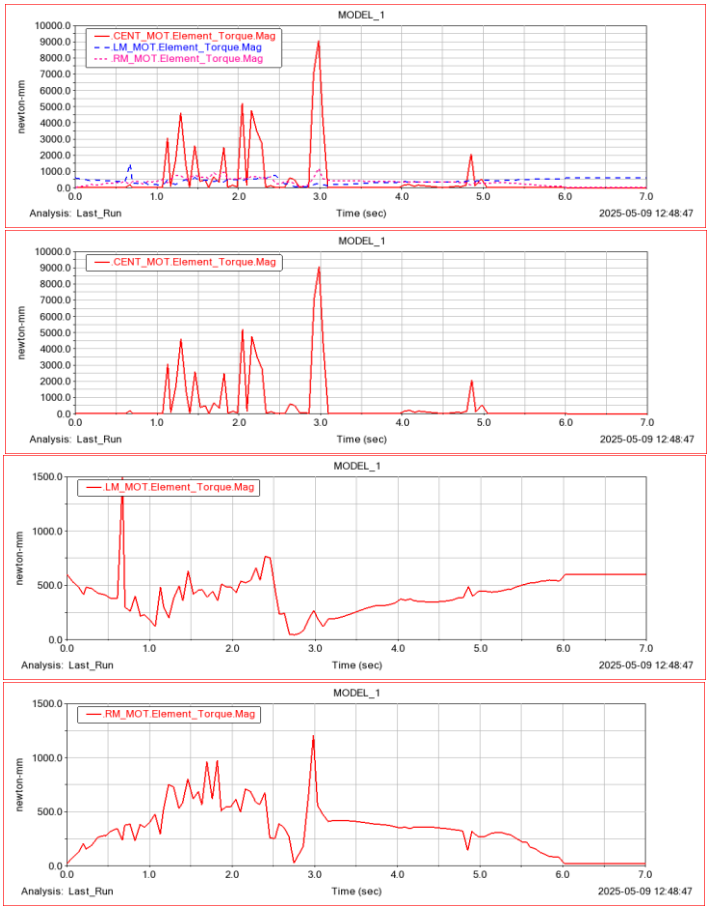

Fig 18. Torque plot of each motor (Central, Left, and Right Motors)

Finally, the authors will demonstrate the selection of the motors based on the analysis of the previous simulation results, as shown in Table 1 below. The left motor, with a peak torque of approximately 1500 N·mm, and the right motor, with a peak of 1240 N·mm, are critical for stabilizing lateral movement.

The central motor, responsible for the 360° rotation around the vertical axis, shows a much higher peak torque of 9000 N·mm, reflecting its role in providing rotational movement around the vertical axis. The motor selection process ensures that each motor can handle these specific torque demands and maintain stable, efficient operation throughout the pick-and-place cycle.
Proper motor selection is essential for the overall system to perform optimally in industrial applications.

Table 1. Motor Selection and enhancement accessories

Motor Name	Motor Selection		
	Torque	Motor Type	Torque enhancement
Central_Motor	9 N.m	Stepper NEMA 23 (3 Nm.)	Planetary Gearbox 5:1
Left_Motor	1.5 N.m	Stepper NEMA 23 (3 Nm.)	No need
Right_Motor	1.24 N.m	Stepper NEMA 23 (3 Nm.)	No need

The central motor is a Stepper NEMA 23 with a rated torque of 3 N·m, enhanced by a planetary gearbox with a 5:1 ratio. This configuration provides precise control of the 360° rotation and accommodates the system's torque requirement of 9 N·m. The left motor, also a Stepper NEMA 23 with a rated torque of 3 N·m, is designed to manage lateral movements effectively without additional enhancement. Similarly, the right motor, another Stepper NEMA 23 with a torque of 3 N·m, ensures optimized performance for lateral operations. This carefully selected combination of motors and enhancements guarantees sufficient torque and precise movement, making the system reliable and efficient for pick-and-place tasks in industrial applications.
Based on recent studies [36][37][38][39][40][41], researchers have developed an innovative hybrid serial robot configuration that significantly enhances mobility and expands the workspace. By incorporating an additional serial joint, the robot achieves full 360-degree rotational capability, thereby extending its operational envelope and increasing its flexibility for complex tasks.

7 Conclusion

The pick-and-place simulation of the hybrid serial-parallel robot underscores the critical role of motor coordination in achieving precise and stable performance. Analysis of the angular velocities highlights that the central motor (CENT_MOT), which reaches peaks of up to 300 deg/sec, is essential for primary rotational movement around the vertical axis. Meanwhile, the left (LM_MOT) and right (RM_MOT) motors, with peak velocities of 150 deg/sec and 75 deg/sec, respectively, contribute mainly to lateral stability, providing corrective forces that enhance precision. The torque distribution further validates this pattern, with the central motor demonstrating a significant peak at 9000 N·mm during the initial lifting phase, showcasing its capacity for handling substantial rotational force. In contrast, the lateral motors exhibit lower, stabilizing torque peaks, confirming their role in balancing the load and ensuring steady, accurate operation. The findings underline the importance of motor coordination in hybrid serial-parallel robots, particularly for applications requiring high Speed and minimal error margins. Future work could focus on refining motor specifications and optimizing control strategies, such as enhancing torque allocation and synchronizing angular velocities, to elevate further the robot's efficiency, reliability, and adaptability. Additionally, exploring advanced control algorithms and energy-efficient motor designs could pave the way for even more sophisticated performance in complex industrial tasks. These advancements would solidify the hybrid serial-parallel robot's position as a versatile and indispensable tool in modern automated manufacturing and material handling systems. Building on these findings, the research team plans to construct a prototype using industrial-grade materials, such as aluminum, as indicated by the simulations. The selection of motors will align with the simulation results, ensuring optimal torque and velocity specifications for reliable and efficient operation.
This prototype will serve as a practical validation of the simulation outcomes, showcasing the robot's capability to handle industrial requirements effectively.

References

1. Zhang, Z., Zhao, X., & Liang, Y. (2023). Design and analysis of a five-DOF hybrid robot with a compliant wrist for machining applications. *ASME Journal of Mechanisms and Robotics*, 15(3), 031002.
2. Ji, W., & Wang, L. (2019). Industrial robotic machining: A review. *International Journal of Advanced Manufacturing Technology*, 103(1-4), 1239–1255.
3. Yue, W., Liu, H., & Huang, T. (2022). An approach for predicting the stiffness of a 5-DOF hybrid robot for friction stir welding. *Mechanism and Machine Theory*, 175, 104941.
4. Pham, M.T., & Dubourg, L. (2016). Impact and improvement of tool deviation in friction stir welding with real-time compensation on an industrial robot. *Robotics and Computer-Integrated Manufacturing*, 39, 22–31.
5. Verl, A., Valente, A., Melkote, S., et al. (2019). Robots in machining. *CIRP Annals - Manufacturing Technology*, 68(2), 799–822.
6. Slavkovic, N.R., Milutinovic, D.S., & Glavonjic, M.M. (2014). Method for off-line compensation of cutting force-induced errors in robotic machining by tool path modification. *International Journal of Advanced Manufacturing Technology*, 70(9-12), 2083–2096.
7. Vihtonen, L., Puzik, A., & Katajarinne, T. (2008). Comparing robot-assisted incremental forming methods: Incremental forming by pressing and incremental hammering. *International Journal of Material Forming*, 1, 1207–1210.
8. Li, X., Yang, B., & Shen, X. (2021). Energy-efficient actuation in hybrid robots: Torsional springs and recuperative drives. *IEEE Transactions on Industrial Electronics*, 68(11), 11190–11198.
9. Ida, E., & Carricato, M. (2024). Static workspace computation for underactuated cable-driven parallel robots. *Mechanism and Machine Theory*, 193, 105551.
10. Birlescu, I., Tohanean, N., Neguran, D., Horsia, A., Vaida, C., Tucan, P., Gherman, B., Condurache, D., & Pisla, D. (2024). Modeling and analysis of a parallel robotic system for lower limb rehabilitation with a predefined operational workspace. *Mechanism and Machine Theory*, 193, 105551.

11. Asada, H., & Slotine, J.-J. (2018). Robot Analysis and Control. *Wiley*.
12. Zhang, J., & Song, J. (2020). Geometric optimization of parallel robots: A Taguchi-based approach. *Journal of Mechanisms and Robotics*, 12(5), 051004.
13. Yang, X., Zhao, Q., & Li, Y. (2023). Dynamic modeling and control of hybrid mechanisms for precision industrial tasks. *Mechanical Systems and Signal Processing*, 198, 109544.
14. Khalil, W., & Dombre, E. (2002). Modeling, Identification, and Control of Robots. *Hermes Penton Science*.
15. Huang, C., & Yang, H. (2021). Kinematic and dynamic analysis of a hybrid 5-DOF robot for precision assembly tasks. *International Journal of Robotics and Automation*, 36(4), 432–439.
16. Meijer, J., Duin, S., & Rooij, R. (2020). Design optimization of a hybrid parallel robot for increased agility in complex industrial tasks. *IEEE Robotics and Automation Letters*, 5(3), 4105–4112.
17. Ni, Y., Jin, M., & Yang, W. (2018). Modeling and simulation of a 3-DOF hybrid manipulator for high-speed material handling. *Mechanics Based Design of Structures and Machines*, 46(4), 438–450.
18. Chen, Z., Zhang, J., & Lin, Y. (2019). Workspace analysis and kinematic optimization of a hybrid serial-parallel robotic arm for industrial pick-and-place operations. *Journal of Mechanisms and Robotics*, 11(5), 054502.
19. Meng, L., Zeng, Q., & Wu, H. (2021). Torque analysis and control optimization of hybrid robots for energy-efficient industrial applications. *IEEE Transactions on Industrial Electronics*, 68(10), 10120–10128.
20. Kim, S., Park, Y., & Lee, D. (2022). Actuator selection and control strategy for dynamic balancing in hybrid robotic systems. *Mechatronics*, 86, 102720.
21. Bai, J., & Wu, R. (2017). Advanced control approaches in hybrid serial-parallel robots for adaptive performance in manufacturing. *Journal of Manufacturing Processes*, 29, 303–312.
22. Sun, H., Zhang, X., & Li, F. (2020). Energy-efficient design and trajectory planning for a hybrid robot performing industrial assembly. *Control Engineering Practice*, 97, 104362.
23. Li, X., Yang, B., & Shen, X. (2021). Energy-efficient actuation in hybrid robots: Torsional springs and recuperative drives. *IEEE Transactions on Industrial Electronics*, 68(11), 11190–11198.
24. Khalil, W., & Dombre, E. (2002). Modeling, Identification, and Control of Robots. *Hermes Penton Science*.
25. Ida, E., & Carricato, M. (2024). Static workspace computation for underactuated cable-driven parallel robots. *Mechanism and Machine Theory*, 193, 105551.
26. Birlescu, I., et al. (2024). Modeling and analysis of a parallel robotic system for lower limb rehabilitation. *Mechanism and Machine Theory*, 193, 105551.
27. Meijer, J., Duin, S., & Rooij, R. (2020). Design optimization of a hybrid parallel robot. *IEEE Robotics and Automation Letters*, 5(3), 4105–4112.
28. Ni, Y., Jin, M., & Yang, W. (2018). Modeling and simulation of a 3-DOF hybrid manipulator. *Mechanics Based Design of Structures and Machines*, 46(4), 438–450.
29. Kim, S., Park, Y., & Lee, D. (2022). Actuator selection and control strategy. *Mechatronics*, 86, 102720.
30. Bai, J., & Wu, R. (2017). Advanced control approaches in hybrid serial-parallel robots. *Journal of Manufacturing Processes*, 29, 303–312.
31. Sun, H., Zhang, X., & Li, F. (2020). Energy-efficient design and trajectory planning. *Control Engineering Practice*, 97, 104362.
32. Khalil, W., & Dombre, E. (2002). Modeling, Identification, and Control of Robots. *Hermes Penton Science*.
33. Zhang, Z., Zhao, X., & Liang, Y. (2023). Design and analysis of a five-DOF hybrid robot. *ASME Journal of Mechanisms and Robotics*, 15(3), 031002.
34. L. Vathan.B, H. Kumar and B. I. John. H, “Kinematic Analysis of Five-Bar Mechanism in Industrial Robotics”.
35. S. Yanli, L. Yanli, W. Hongtao, H. Chunlong, and W. Shuai, “Forward and Inverse Kinematics for a Novel Double Scara Robot,” in 2nd International Symposium on Resource Exploration and Environmental Science, 2018.
36. H. Guo, "Design and Experiment of a Safflower Picking Robot Based on a Parallel Manipulator," Feb. 2022.
37. M. D. Ratolikar, "Optimization of 5R Planar Parallel Mechanism Dimensions Using Genetic Algorithm for Reduced Peak Torque," Jan. 2022.

38. H. Cervantes-Culebro, "Concurrent Optimal Design of a Planar Five-Bar Parallel Robot for High-Speed Pick and Place Tasks," Jan. 2021.
39. Elsamanty, M., Faidallah, E. M., Hossameldin, Y. H., Rabbo, S. A., Maged, S. A., Yang, H., & Guo, K. (2023). *Workspace Analysis and Path Planning of a Novel Robot Configuration with a 9-DOF Serial-Parallel Hybrid Manipulator (SPHM)*. *Applied Sciences*, 13(4), 2088. https://doi.org/10.3390/app13042088
40. Elkholy, H. A., Shahin, A. S., Shaarawy, A. W., Marzouk, H., & Elsamanty, M. (2020). *Solving Inverse Kinematics of a 7-DOF Manipulator Using Convolutional Neural Network*. In A. E. Hassanien, A. Azar, T. Gaber, D. Oliva, & F. Tolba (Eds.), *Proceedings of the International Conference on Artificial Intelligence and Computer Vision (AICV2020)* (Vol. 1153, pp. 385–393). Springer, Cham. https://doi.org/10.1007/978-3-030-44289-7_32
41. Elsamanty, M., Faidallah, E. M., Hossameldin, Y. H., Abd Rabbo, S. M., & Maged, S. A. (2021). *Design, Simulation, and Kinematics of 9-DOF Serial-Parallel Hybrid Manipulator Robot*. In *2021 3rd Novel Intelligent and Leading Emerging Sciences Conference (NILES)* (pp. 370–375). IEEE. https://doi.org/10.1109/NILES53778.2021.9600537
42. Asy, K. M., Zaky, A. B., El-Hussieny, H., Ishii, H., & Elsamanty, M. (2023). *Conceptual Design and Kinematic Analysis of a Hybrid Parallel Robot for Accurate Position and Orientation*. In *2023, the 62nd Annual Conference of the Society of Instrument and Control Engineers (SICE)* (pp. 558–563). IEEE. https://doi.org/10.23919/SICE59929.2023.10354230